



Neutron elastic and inelastic scattering differential cross sections on carbon

A.P.D. Ramirez^{a,b}, E.E. Peters^a, J.R. Vanhoy^{c,*}, S.F. Hicks^{d,b},
L.A. Alasagas^c, D.K. Alcorn-Dominguez^c, S.T. Block^d, S.T. Byrd^d,
E.A. Chouinard^d, B.M. Combs^d, B.P. Crider^b, E.C. Deryn^d,
L. Downes^d, J.A. Erlanson^c, S.E. Evans^d, A.J. French^d, E.A. Garza^c,
J. Girgis^d, T.D. Harrison^c, S.L. Henderson^d, T.J. Howard^d,
D.T. Jackson^d, L.J. Kersting^d, A. Kumar^a, S.H. Liu^a, C.J. Lueck^d,
E.M. Lyons^d, P.J. McDonough^d, M.T. McEllistrem^{b,1}, T.J. Morin^d,
S. Mukhopadhyay^b, T.A. Nguyen^d, M. Nickel^d, S. Nigam^a, R.L. Pecha^d,
J. Potter^a, F.M. Prados-Estévez^{a,b}, B.G. Rice^c, T.J. Ross^{a,b},
Z.C. Santonil^d, J. Schneiderjan^d, L.C. Sidwell^d, A.J. Sigillito^d,
J.L. Steves^c, B.K. Thompson^c, D.W. Watts^c, Y. Xiao^{a,b},
S.W. Yates^{a,b}

^a Department of Chemistry, University of Kentucky, Lexington, KY 40506-0055, USA

^b Department of Physics and Astronomy, University of Kentucky, Lexington, KY 40506-0055, USA

^c Department of Physics, United States Naval Academy, Annapolis, MD 21402-5026, USA

^d Department of Physics, University of Dallas, Irving, TX 75062-4736, USA

Received 25 March 2022; accepted 30 March 2022

Available online 5 April 2022

Abstract

Elastic and inelastic neutron scattering angular distributions were measured on natural carbon samples to confirm existing experimental data and evaluations in the fast neutron region and to guide improvements

* Corresponding author.

E-mail addresses: ramirez112@llnl.gov (A.P.D. Ramirez), vanhoy@usna.edu (J.R. Vanhoy), hicks@udallas.edu (S.F. Hicks).

¹ Deceased.

in resonance parameters, where needed. Sixty-four (n,n') differential cross section measurements were performed at 45 incident neutron energies between 0.5 and 8.0 MeV.

Experimental angle-integrated elastic scattering cross sections are consistent with ENDF/B-VIII.0 values with the exception of the region from 3.2 to 4.0 MeV where our results are $\sim 3\%$ higher. In the 3.4 to 3.6 MeV region our differential cross sections are slightly lower at forward angles and somewhat higher at backward angles than the ENDF/B-VIII.0 calculations; however, our results are consistent with measured data from other research groups. The first- through fourth-order elastic scattering Legendre coefficients from fits to these experimental data are consistent with ENDF/B-VIII.0 values across this range of incident neutron energies.

Inelastic scattering cross sections were measured at 12 incident neutron energies between 5.6 and 7.8 MeV. Angle-integrated cross sections agree well with the 1978 Perey and ENDF/B-VIII.0 values; however, the angular-distribution shapes deviate somewhat from the ENDF/B-VIII.0 calculations. These data will allow refinement of the resonance parameter description in this difficult energy region.

Published by Elsevier B.V.

Keywords: Neutron elastic and inelastic scattering; Differential cross sections; $^{nat}\text{C}(n,n')$; Legendre coefficients

1. Introduction

Carbon-12 is under development as a fast neutron scattering cross section reference standard, as it is readily available in high purity, and it occurs in many compounds. The average isotopic fractions are 0.9890 ^{12}C and 0.0110 ^{13}C with variations in the ^{13}C fraction of $< \pm 0.0005$ [1]. The total cross sections in the range from 10 eV to 1.8 MeV are already considered a reference standard and were recently reviewed by Carlson et al. [2], who retained the values from the earlier evaluation [3].

Hale and Young [4] updated the R-matrix description of the ^{13}C system resulting in a new evaluation of neutron cross sections for ^{12}C up to about 6.5 MeV. Uncertainties in the angle-integrated elastic cross sections range from 0.3% at 1 MeV to 4% at 6.5 MeV. Inelastic scattering populating the 4.44 MeV first excited state is not as well described.

Most nuclear data libraries have been recently updated. The ENDF/B-VIII.0 release [5] of February 2018 incorporates the best values [4] and for the first time presents the isotopic ^{12}C and ^{13}C cross sections. The previous ENDF/B-VII.1 release only presented elemental carbon recommended values. The JEFF-3.3 evaluated library of November 2017 contains only elemental carbon. The January 2016 update of the JENDL-4.0u library retained former values for neutron scattering on elemental carbon.

In neutron scattering measurements at the University of Kentucky Accelerator Laboratory (UKAL), carbon is regularly used for a check of our procedures and analyses. Quick measurements of ^{nat}C elastic scattering angular distributions were consistent with previous data [6], except at a few energies. From MCNP simulations of our experimental conditions, we realized that peaks in the neutron time-of-flight (TOF) spectra could not always be modeled as a Gaussian (or variant) with an exponential or linear tail. At some angles, multiple scattering in the sample generates a wide, low shelf in the spectra that contains appreciable yield. We examined spectra available from the doctoral thesis and notes of Galati [7] from early neutron scattering studies at UKAL; these low-energy shelves were not recognized as separate from general background events at the time.

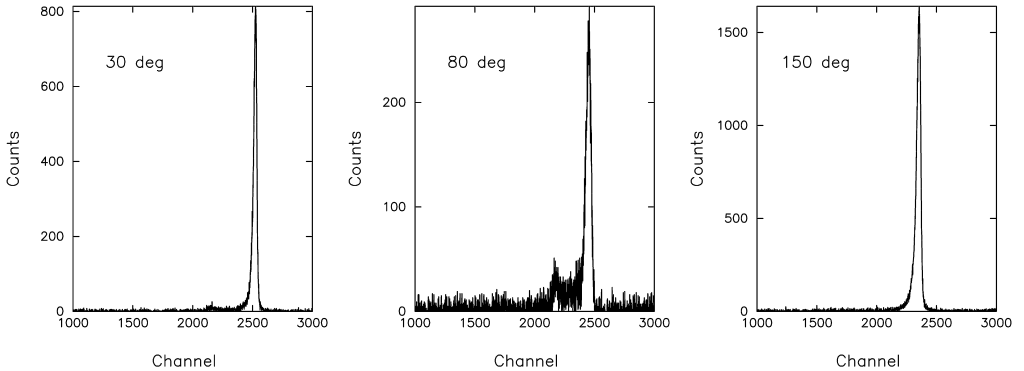


Fig. 1. Measured TOF spectra for 3.8 MeV neutrons on elemental carbon. The 30° and 80° spectra exhibit features to the left of the main TOF peak. This low-energy shelf arises from multiple scattering and random background; it is more apparent in the 80° spectrum because of the small elastic scattering differential cross section at that angle.

Similarly, the published references by Fasoli [6], Lane [8], Drigo [9], Langsdorf [10], and Elwyn [11] from the 1950s and 1969-1973 eras were investigated. Few TOF spectra are presented in those studies, and there is no discussion of the peak-fitting techniques used. The TOF spectra from those eras have only a few points spanning each peak, and there is a significant background underlying the peaks. Published figures suggest the peak yields were extracted by summing counts above a linear background. This procedure is not surprising as fifty years ago fewer tools and techniques were available. To investigate neutron scattering from ^{nat}C in a consistent way, we began an extensive measurement program of angular distributions at 45 energies between 0.3 and 8 MeV. Examples of spectra from the present measurements at $E_n = 3.8$ MeV are shown in Fig. 1.

2. TOF spectra modeling for multiple scattering effects

MCNP simulations that included details of neutron production in the gas cell (energy and angular dependencies), proper geometries and construction details for the end of the beamline, scattering sample location, and neutron detector collimation were performed. Scattered neutron energy spectra were generated as a function of scattering angle. Simulated spectra for $E_n = 4.0$ MeV at 30° , 80° , and 150° are shown in Fig. 2.

Double scattering events in the 150° spectrum shift the energy only slightly and the main effect is energy broadening. The 150° peak can be fitted with a typical Gaussian plus tail to account for all the scattering yield. We conclude that at backward angles a negligible portion, $<1\%$, of the true scattered yield is missed.

Carbon differential cross sections tend to have a minimum near 90° , therefore multiple scattering effects are more apparent in the 80° panels of Fig. 2. Those multiple scattering events are spread over a 2 MeV energy range in the spectrum and triple scattering events are noticeable. These events are evident as a wide shelf in the top 80° panel. The bottom cumulative yield panel indicates $\sim 17\%$ of the scattering yield would be neglected at 80° if the TOF peak were fitted with a traditional Gaussian plus tail function. Improperly accounting for and correcting for multiple scattering would have a large effect in this example.

A similar situation occurs in the 30° spectrum in Fig. 2. The wide shelf is barely noticeable in the top panel; however, ignoring this feature would neglect $\sim 5\%$ of the scattered yield. Under

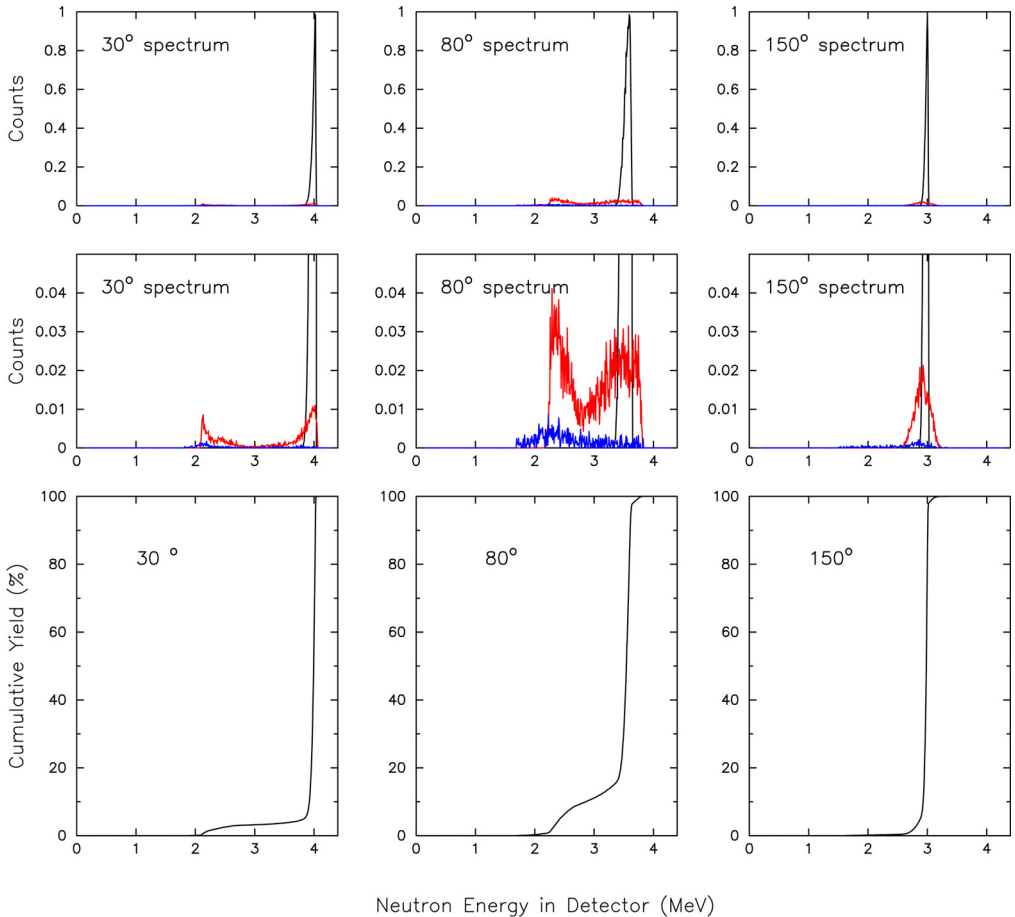


Fig. 2. Simulated scattered neutron energy spectra for 4.0 MeV neutrons on elemental carbon. Contributions from single scattering and multiple scattering in the sample are indicated separately. Single scattering is indicated in black, double scattering in red, and triple scattering in blue. The top row of panels displays the whole spectrum scaled to the peak height. The second row is expanded to 5% of the peak height to illustrate the multiple scattering components. The bottom row of panels indicates the fraction of the scattering yield up to the energy, E , in the spectrum. (For interpretation of the colors in the figure, the reader is referred to the web version of this article.)

estimations of the scattered yield caused by neglecting multiple scattering will result in under estimations of the true differential cross sections. The problem is most severe at angles from 70° to 90° .

Because measurements at the UKAL have traditionally focused on heavy nuclei, we repeated the simulation for an ^{56}Fe target for comparison. The double- and triple-scattering effects still exist in the ^{56}Fe TOF spectra but do not appear as an extended shelf; the observed peak shape can be interpreted as a Gaussian plus short exponential tail and all of the scattered yield is recovered. The conclusion is that spectra for significantly heavier mass nuclei do not suffer from this issue because of the smaller recoil energies.

Although our multiple scattering code, MULCAT, is well-trusted for heavier nuclei, our desire to produce the highest quality ‘nuclear data’ has lead us to test its accuracy. To date, we have

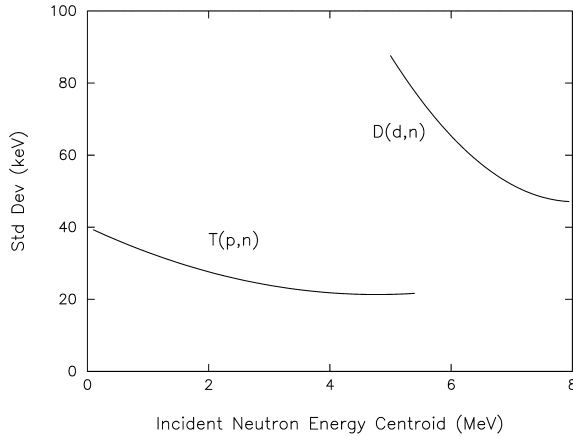


Fig. 3. Energy spreads of incident neutrons across the face of the carbon sample, measured in standard deviations (Std Dev), as modeled by NeuSDesc [16] incorporating SRIM stopping powers [17] for the range of E_n used in these measurements.

performed chained MCNP-MULCAT calculations. The MCNP portion of the simulation uses ENDF values to generate simulated experimental yields. Cross sections derived from those yields were then processed through the MULCAT correction to reproduce the original ENDF values used by MCNP. The values returned are within 2-5% of the ENDF values.

3. Methods

The equipment, methods, and data reduction techniques employed at UKAL are discussed extensively in several papers [12–15]. The laboratory features a single-ended 7 MV model CN Van de Graaff accelerator with a terminal-based bunching system. The pulsed proton or deuteron beams have a time spread of ~ 1 ns at the neutron production target. The ${}^3\text{H}(p,n){}^3\text{He}$ and ${}^2\text{H}(d,n){}^3\text{He}$ reactions were employed to produce the source neutrons below and above 4.5 MeV, respectively. The energy spreads of the neutrons impinging over the area of the sample as estimated by the code NeuSDesc [16] including SRIM stopping powers [17] are illustrated in Fig. 3.

Neutron production is measured using time-of-flight (TOF) techniques with forward monitor (FM) detectors containing NE-213 or C_6D_6 scintillation fluids. A FM is placed at 45° with respect to the incident beam direction and above the scattering plane to provide a direct, collimated view of the gas cell during measurements. When the ${}^2\text{H}(d,n){}^3\text{He}$ reaction is used for neutron production, a second FM is placed at 20° and in the scattering plane because a minimum occurs in the neutron production cross section at 45° . Source neutrons are identified in the FM by TOF and pulse-shape discrimination (PSD); the combination of which provides a very clean monitor of on-pulse neutron production.

Scattering samples utilized in these (n,n') and $(n,n'\gamma)$ measurements were right circular cylinders suspended at distances 6.4 to 7.7 cm from the center of the 3 cm long gas cell. The masses and geometries of the samples used are given in Table 1. A small natural carbon sample was chosen to reduce attenuation and multiple scattering contributions and was smaller than the samples used in measurements previously mentioned. A solid polyethylene cylinder was used to measure ${}^1\text{H}(n,n){}^1\text{H}$ cross sections for absolute normalization to a reference standard.

Table 1
Scattering samples.

Sample	Mass (g)	Diameter (cm)	Height (cm)
^{nat}C	10.98	2.01	2.01
polyethylene	1.069	1.94	1.49
^{nat}Ti	44.54	2.23	2.55
99.87% ^{56}Fe	18.18	1.52	1.45
^{nat}V	49.20	1.91	2.84
Al	26.96	2.20	2.54

Scattered neutrons were detected with an 11.5 cm diameter \times 2.5 cm thick C_6D_6 main detector, which permitted PSD rejection of γ -ray events. An identically constructed detector of 5.0 cm thickness was used during higher energy measurements with the $^2\text{H}(d,n)^3\text{He}$ neutron production reaction. The detector was mounted on a goniometer that can be rotated to cover detection angles up to 155° with respect to the incident beam direction. The goniometer supports a full-length collimation system with flight paths up to 4 m.

In view of the discussion in Section 2, special care was taken in determining elastic scattering yields. Sample-out TOF spectra were subtracted from sample-in spectra and the resulting TOF spectra were scrutinized. The carbon elastic scattering yield was extracted with both our standard in-house Gaussian(s) plus tail(s) fitting program SAN12 and a simple counts-above-a-linear-background technique. SAN12 incorporates kinematic constraints on peak positions, widths, and tails. The spectra and fits were examined individually, and a best value and uncertainty was chosen.

At incident energies above 5 MeV, the carbon inelastic channel is open, and the yield of the inelastic peak must be fitted with the counts-above-a-linear-background technique because the peak is significantly Doppler broadened.

While the (n,n_1) peak is well separated from the elastic peak, care must be taken at the most forward angles to assure that counts from the tail of the much more intense elastic peak are not attributed to the yield of the inelastic peak. Even with extra care, the uncertainty of the (n,n_1) yield increases at angles $<40^\circ$ because small changes in the elastic peak's left tail are magnified due to the large forward-angle elastic scattering differential cross section.

The C_6D_6 detector efficiency (Fig. 4) is determined by direct measurement of the source reaction angular distribution and its associated kinematics. We measure rather than model the efficiency because the sample and gas cell are close; the neutron fluence emerging from the gas cell is divergent; and the energies of the inelastic reactions are just above the detector threshold. The $d\sigma/d\Omega_{Tpn}$ cross sections are taken from the DROSG-2000 program series [18,19]. Our cross section normalization technique is not sensitive to the magnitude of the $^3\text{H}(p,n)^3\text{He}$ or $^2\text{H}(d,n)^3\text{He}$ cross sections, only their angular dependence. Uncertainties in the angular dependence of these cross sections, approximately 3%, are among the largest contributors to the overall uncertainty in the measured neutron scattering cross sections.

Cross sections are normalized absolutely using the recommended values for the $^1\text{H}(n,n)$ total cross sections taken from Tables XVIII and XIX of Ref. [20] and Ref. [21]. Both references provide the same absolute angle-integrated $^1\text{H}(n,n)$ values which are known to $\pm 0.30\%$ or better in the energy range of our measurements. The differential cross sections in the center-of-mass system vary by $\pm 0.5\%$ from the isotropic estimate, which is much smaller than the uncertainties

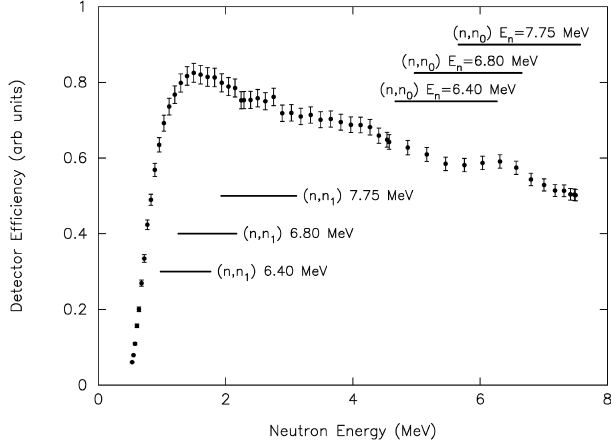


Fig. 4. A representative main detector efficiency curve used for measurements at 6.40, 6.50, 6.80, 7.25, and 7.75 MeV. The location and shape of the sharp rise in the curve is due to lower level discriminator settings in the electronics. Horizontal bars indicate the range of scattered neutron energies of the indicated reactions from 30° to 150° .

incurred in the detector efficiency. Because of the small discrepancy, we consider $d\sigma/d\Omega$ to be isotropic in the center-of-mass frame.

Measured differential cross sections are corrected for attenuation and multiple scattering effects in the sample, taking into account the close cell-to-sample geometry with the code MULCAT [22]. The code performs an iterative Monte Carlo calculation, taking as input the uncorrected experimental differential cross sections and using them along with known total cross sections and information for the source reaction to estimate the corrected differential cross sections. MULCAT then repeats this process, using now the estimated cross sections as input; the whole process is iterated until the differential cross sections converge. Uncertainties in the attenuation and multiple scattering corrections are less than 5%.

3.1. γ -ray measurements

Eight γ -ray angular distributions were measured using the $(n,n'\gamma)$ reaction. The γ rays were detected using a Compton-suppressed n-type HPGe detector with 51% relative efficiency and an energy resolution of 2.1 keV FWHM at 1.33 MeV. A bismuth germanate (BGO) annular detector surrounding the main detector was used for Compton suppression and as an active shield. The gain stability of the system was monitored using a radioactive ^{226}Ra source, which was also used for energy and efficiency calibrations. The γ -ray spectra were cleansed of scattered neutron events by gating the ADC on prompt γ rays in the TOF spectrum. Details of γ -ray techniques used at UKAL are described in Ref. [15]. Yields of the 4440 keV γ ray from neutron inelastic scattering from ^{12}C were converted to cross sections using ^{56}Fe , ^{48}Ti , ^{51}V , and ^{27}Al cross sections as references.

4. Observations

All measurements utilized a natural carbon target. For elastic scattering, the neutron TOF peaks for ^{12}C and ^{13}C are unresolved. The natural abundance of ^{13}C is $1.10 \pm 0.05\%$, and the

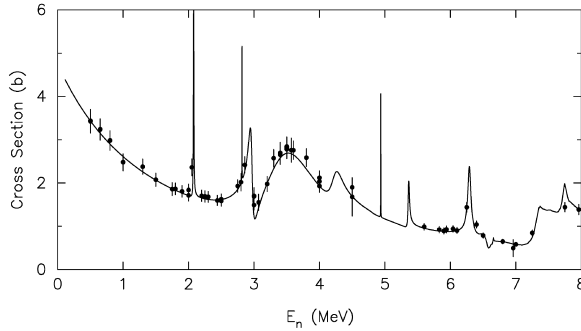


Fig. 5. Comparison of our ^{nat}C angle-integrated elastic cross sections (\bullet) with ENDF/B-VIII.0 values (line) [5].

^{13}C contribution will only significantly affect the elastic scattering results where the ^{13}C cross section is large. In general, this is a 1.0% effect except in the range of incident neutron energies from 5.5 to 7.3 MeV where the ^{12}C cross section is smallest. Cross section values are quoted for a natural carbon target for elastic scattering.

4.1. Elastic scattering

Neutrons with energies of a few MeV lie in the resolved resonance region for carbon; cross sections in that region are well explained with an R-matrix treatment. If the required resonance energies and partial widths are generated solely by fits to angle-integrated or total cross sections, knowledge of the individual partial width amplitudes can be masked. Experimental angular distributions place rigorous constraints on these amplitudes. The angle-integrated elastic cross sections (Fig. 5) are determined from Legendre polynomial fits to the differential cross sections displayed in Figs. 6 and 7.

Agreement between the elastic cross sections and the ENDF/B-VIII.0 compilation is very good, with the exception of the region around 3.5 MeV where our values for the cross sections are $\sim 3\%$ higher. A comparison of our results with those of other research groups in that region is shown in Fig. 6. Our forward-angle $d\sigma/d\Omega$ tends to be higher than data from the Fasoli 1973 measurements [6].

It is convenient to examine the angular distributions in terms of the Legendre expansion coefficients a_L^{ENDF} , where

$$\frac{d\sigma}{d\Omega} = \frac{\sigma_s}{2\pi} \sum_L \frac{2L+1}{2} a_L^{ENDF} P_L(\cos\theta) \quad (1)$$

defines the expansion coefficients in the ENDF convention. This approach greatly magnifies variations in the angular distributions. Legendre coefficients as a function of energy for $^{12}\text{C}(n, n_0)$ are shown in Fig. 8. These coefficients are very sensitive to the theoretical model description. A similar analysis was performed previously by Lane [8].

The Legendre coefficients follow the ENDF/B-VIII.0 values very well. The large a_2 coefficient in the 2.5 to 4.0 MeV region reflects the symmetry observed in the angular distributions about 90° in Fig. 7. The illustration confirms that the resonance parameters selected for the elastic channel [4] describe the elastic angular distributions and interference between resonances

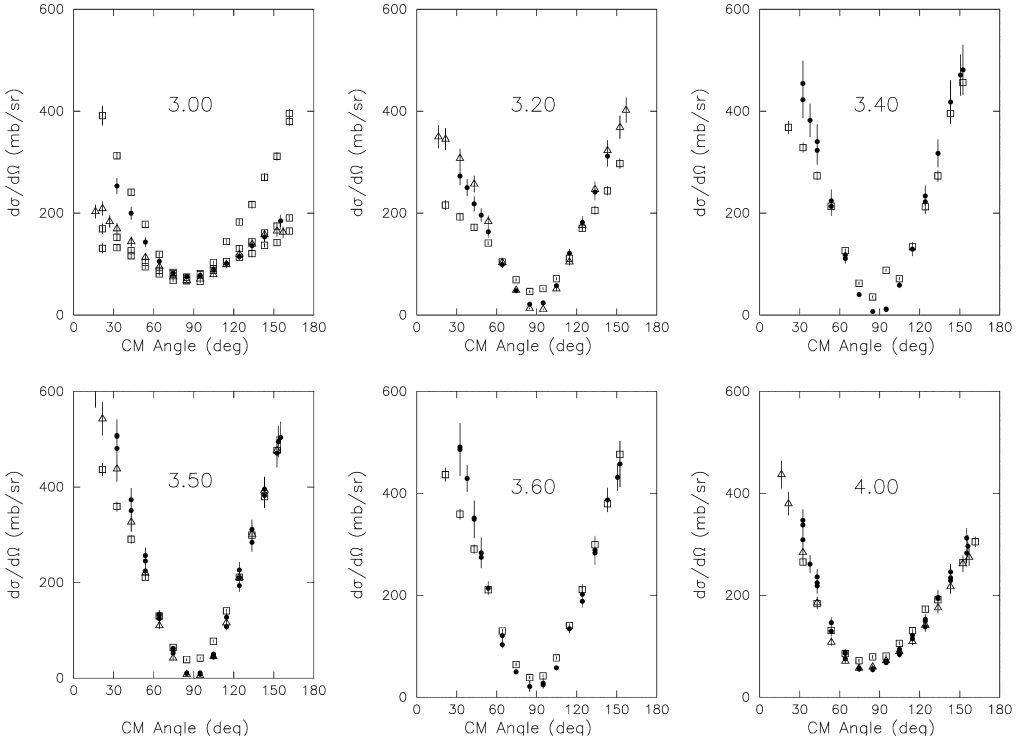


Fig. 6. Comparisons of measured ^{nat}C elastic scattering cross sections in the $E_n=3.0$ to 4.0 MeV region. Values are from Fasoli (\square) [6], Galati (Δ) [7], and our results (\bullet). $E_n=3.00$ MeV is in the bottom of a sharp resonance feature in the neutron total cross sections and differences are expected. Data shown span a range of 70 keV, and the sensitivity to the exact neutron energy is apparent. The $E_n=3.20$ MeV results are in a smoother varying region of the total cross sections. Data shown span a range of 70 keV. The present results and those of Galati [7] are consistent but have a sharper shape than Fasoli [6]. The $E_n = 3.40 - 3.60$ MeV panels cover a local increase in the cross sections. Data shown span a range of not more than 40 keV. All three references are consistent, but the present results and those of Galati [7] tend to be significantly higher at forward angles. The $E_n = 4.00$ MeV panel is above the discrepant region and results from the three research groups are in excellent agreement.

very well. Since the elastic scattering is from a spin-0 nucleus, only one (s, l) neutron partial width is required per resonance.

4.2. Inelastic scattering

In contrast with the elastic data, the $^{12}\text{C}(n, n_1)$ channel is not as well known, with significant differences reported among previous measurements for angle-integrated cross sections. This discrepancy is a serious problem for a resonance reaction model description of the inelastic scattering because three (s, l) exit channels are active per resonance, and it is difficult to determine the partial widths without measured angular distribution data.

Measurements below $E_n = 5.5$ MeV become very time consuming as the 0-degree $^2\text{H}(d, n)^3\text{He}$ production cross section drops to <30 mb/sr, and it is difficult to compensate with increased pressure in the gas cell. In addition, while the n_1 and n_0 peaks are well separated in the TOF spectra, the reaction kinematics specific to ^{12}C and its first excited state prove challenging because the

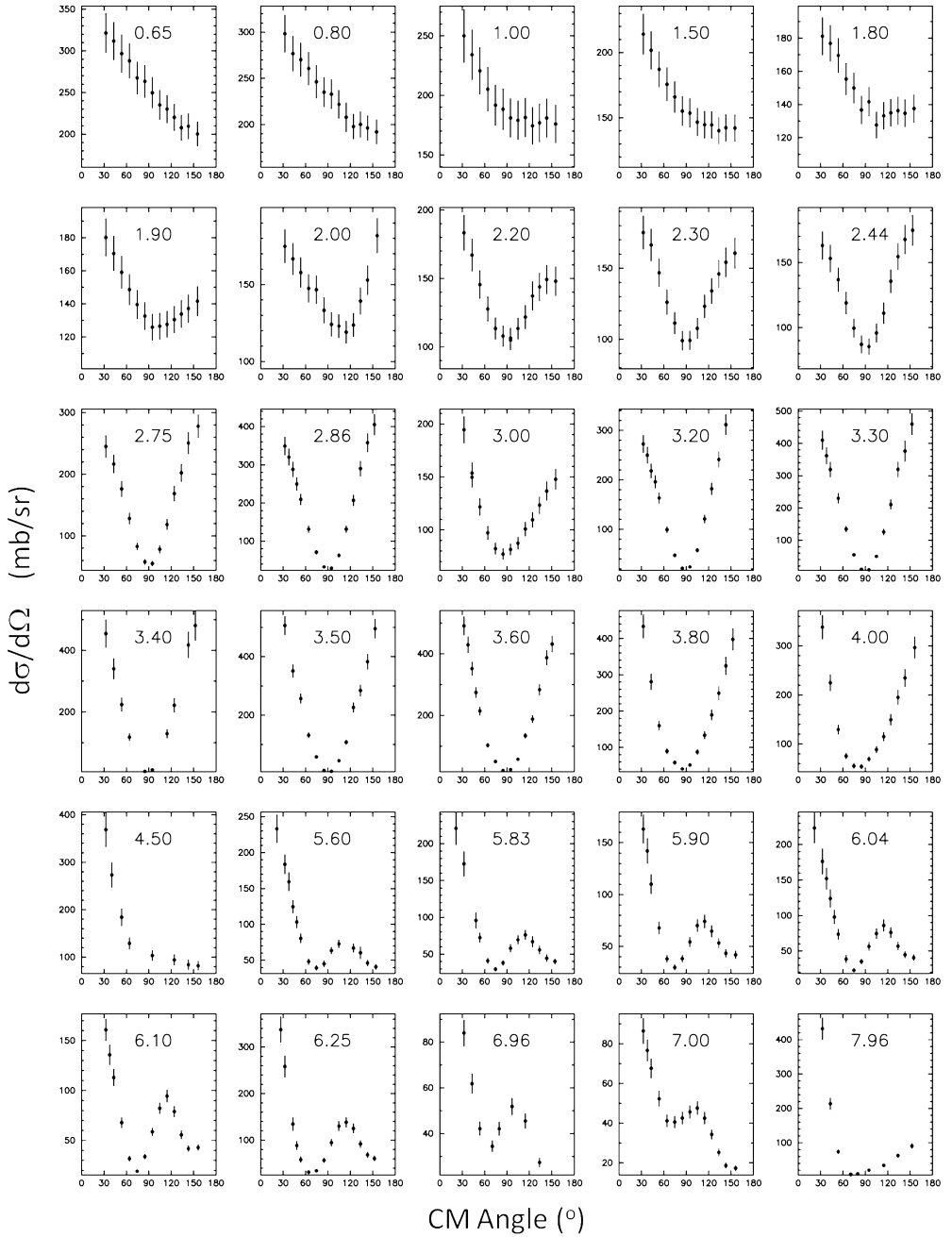


Fig. 7. A representative collection of measured neutron elastic scattering differential cross sections (mb/sr) for ^{nat}C versus angle ($^\circ$) in the center-of-mass frame. The lowest energies are reminiscent of potential scattering, with the onset of resonance behavior at ~ 2.0 MeV. The shapes transition back to more optical model diffractive cross sections just above 4.0 MeV, with resonance features reappearing about 7.0 MeV.

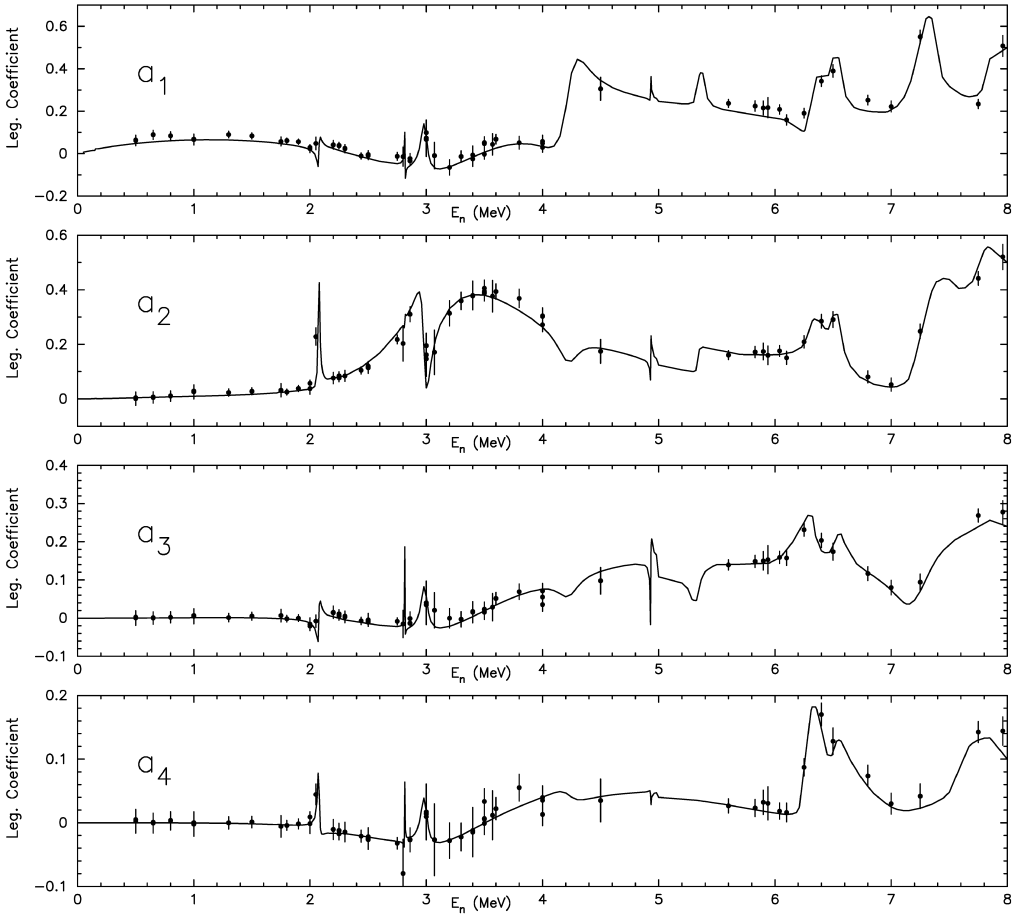


Fig. 8. Measured Legendre coefficients for neutron elastic scattering (●) compared to coefficients from the ENDF/B-VIII.0 ¹²C compilation (solid line). Statistical uncertainties are displayed.

scattered neutron energy changes significantly with scattering angle, and measuring the detector efficiency over this large range is difficult.

Values for the angle-integrated inelastic cross sections shown in Fig. 9 are derived from Legendre fits to the differential cross sections shown in Fig. 10 and agree well with the ENDF/B-VIII.0 values.

The angular distributions below 6.1 MeV are slowly varying as no strong narrow resonances are identified, and our results are reasonably consistent with the ENDF/B-VIII.0 values. Several very sharp resonances occur in the 6.2 - 6.6 MeV region and it is difficult to match the angular behavior. Our 7.0 MeV angular distribution is again reasonably consistent with the ENDF/B-VIII.0 evaluations in the 7.0 - 7.25 MeV region, but the 7.75 MeV data point is again at a sharp resonance.

In Fig. 11, we display the Legendre coefficient results. The a_2 , a_3 , and a_4 coefficients follow the evaluation and values from other measurements. Our a_1 coefficients are consistent with both the Perey [23] and ENDF values above 6.1 MeV. Both Perey and our values are significantly

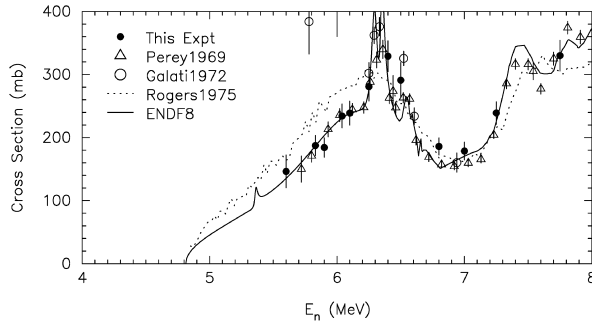


Fig. 9. Comparison of our angle-integrated (n, n_1) inelastic cross sections with the ENDF/B-VIII.0 (ENDF8) and values from EXFOR. The results closely follow the ENDF8 and Perey values [23], but differ from the Galati [7] and Rogers [24] results.

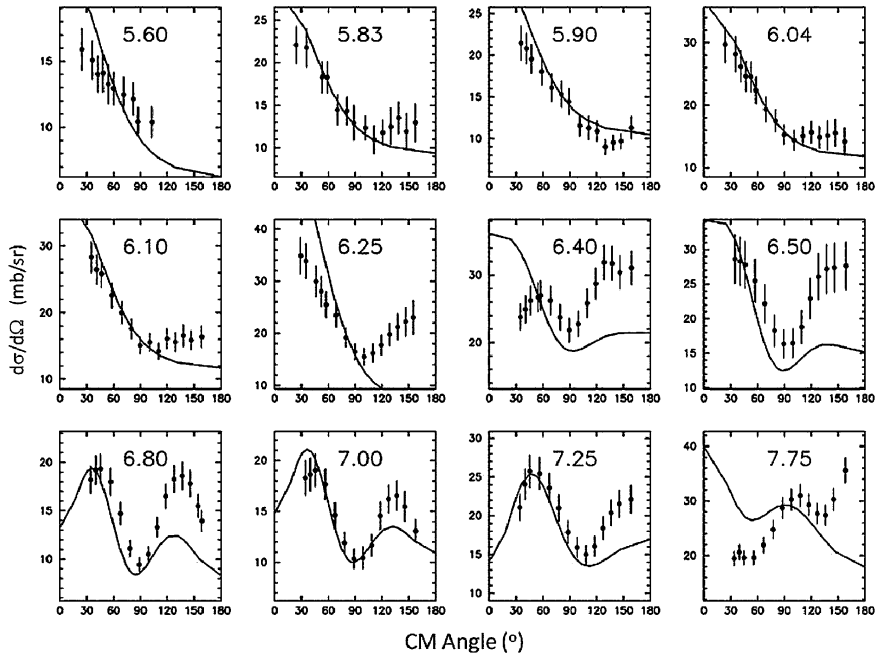


Fig. 10. Inelastic scattering differential cross sections (n, n_1) versus center-of-mass angle for the first excited state in ^{12}C (\bullet) compared to ENDF/B-VIII.0 evaluations (solid line). It is difficult to make conclusions about the agreement because there are a number of sharp resonances in the energy ranges 6.2 to 6.6 MeV and above 7.4 MeV where the angular distribution shape can change rapidly.

greater than the evaluation below 6.1 MeV. Our values are not consistent with the Galati results [7], which were obtained with a much larger carbon scattering sample.

5. Summary

Neutron scattering angular distributions were measured and cross sections extracted for 45 incident neutron energies between 0.5 and 8 MeV on a natural carbon sample. The scattering

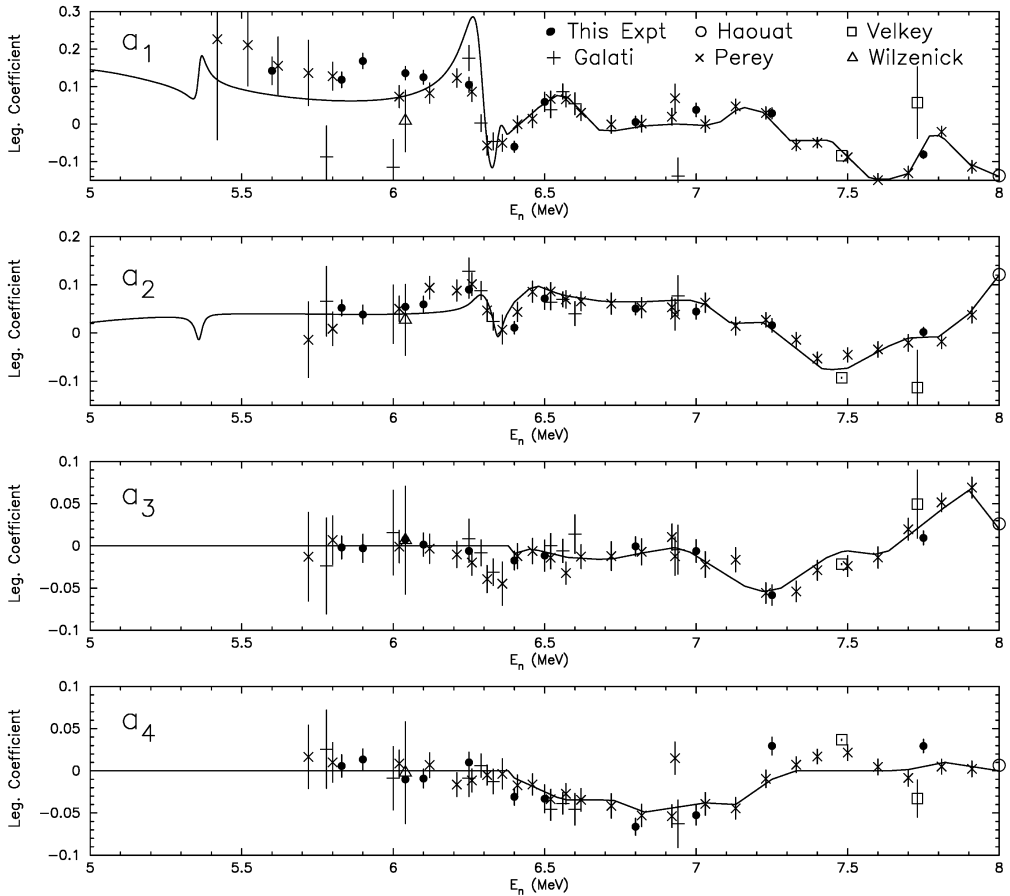


Fig. 11. Legendre coefficients from our measurements of inelastic scattering from the ^{12}C first excited state compared to coefficients from the ENDF/B-VIII.0 compilation (solid line) and previous measurements. Statistical uncertainties are displayed.

sample chosen was smaller than those in previous experiments to reduce attenuation and multiple scattering effects. The data are distributed via EXFOR.

Angle-integrated elastic scattering cross sections are consistent with ENDF/B-VIII.0 values with the exception of the region from 3.2 to 4.0 MeV where our results are 3% higher. In the 3.4 to 3.6 MeV region, our differential cross sections are slightly lower at forward angles and somewhat larger at backward angles than the ENDF/B-VIII.0 calculations; however, our measurements are consistent with data measured by other research groups. The first- through fourth-order elastic scattering Legendre coefficients are consistent with ENDF/B-VIII.0 values.

Inelastic scattering was measured at 12 incident neutron energies between 5.6 and 7.8 MeV. Angle-integrated cross sections follow the 1969 Perey and ENDF/B-VIII.0 values very well. The measured a_1 Legendre coefficient is higher than the ENDF/B-VIII.0 values in the region below 6.1 MeV. These data will allow refinement of the resonance parameter descriptions in this difficult region.

Declaration of competing interest

The authors declare that they have no known competing financial interests or personal relationships that could have appeared to influence the work reported in this paper.

Acknowledgements

Research at the University of Kentucky Accelerator Laboratory is supported by contracts from the U.S. Department of Energy programs NNSA-SSAP award NA-0002931, Nuclear Energy Universities Program award NU-12-KY-UK-0201-05, and the Office of Nuclear Physics awards DE-20SSC000056, DE-SC0021243, DE-SC0021175, and DE-SC0021424. Support also was received from the Donald A. Cowan Physics Fund at the University of Dallas, and in part by the National Science Foundation grant PHY-1913028. Isotope(s) used in this research were supplied by the U.S. Department of Energy Isotope Program, managed by the Office of Isotope R&D and Production. The authors also acknowledge the many contributions of H.E. Baber to these measurements.

References

- [1] T.B. Coplen, Y. Shrestha, IUPAC technical report: isotope-abundance variations and atomic weights of selected elements: 2016, *Pure Appl. Chem.* 88 (12) (2016) 1203–1224, <https://doi.org/10.1515/pac-2016-0302>.
- [2] A.D. Carlson, V.G. Pronyaev, R. Capote, G.M. Hale, Z.-P. Chen, I. Duran, F.-J. Hamsch, S. Kunieda, W. Mannhart, B. Marcinkewicz, R.O. Nelson, D. Neudecker, G. Noguere, M. Paris, S.P. Simakov, P. Schillebeeckx, D.L. Smith, X. Tao, A. Trkov, A. Wallner, W. Wang, *Nucl. Data Sheets* 148 (2018) 143–188, <https://doi.org/10.1016/j.nds.2018.02.002>.
- [3] A.D. Carlson, V.G. Pronyaev, D.L. Smith, N.M. Larson, Z. Chen, G.M. Hale, F.-J. Hamsch, E.V. Gai, Soo-Youl Oh, S.A. Badikov, T. Kawano, H.M. Hofmann, H. Vonach, S. Tagesen, *Nucl. Data Sheets* 110 (12) (2009) 3215–3324, <https://doi.org/10.1016/j.nds.2009.11.001>.
- [4] G.M. Hale, P.G. Young, *Nucl. Data Sheets* 118 (2014) 165–168, <https://doi.org/10.1016/j.nds.2014.04.027>.
- [5] D.A. Brown, M.B. Chadwick, R. Capote, A.C. Kahler, A. Trkov, M.W. Herman, A.A. Sonzogni, Y. Danon, A.D. Carlson, M. Dunn, D.L. Smith, G.M. Hale, G. Arbanas, R. Arcilla, C.R. Bates, B. Beck, B. Becker, F. Brown, R.J. Casperson, J. Conlin, D.E. Cullen, M.-A. Descalle, R. Firestone, T. Gaines, K.H. Guber, A.I. Hawari, J. Holmes, T.D. Johnson, T. Kawano, B.C. Kiedrowski, A.J. Koning, S. Kopecky, L. Leal, J.P. Lestone, C. Lubitz, J.I. Márquez Damián, C.M. Mattoon, E.A. McCutchan, S. Mughabghab, P. Navrátil, D. Neudecker, G.P.A. Nobre, G. Noguere, M. Paris, M.T. Pigni, A.J. Plompen, B. Pritychenko, V.G. Pronyaev, D. Roubtsov, D. Rochman, P. Romano, P. Schillebeeckx, S. Simakov, M. Sin, I. Sirakov, B. Sleaford, V. Sobes, E.S. Soukhovitskii, I. Stetcu, P. Talou, I. Thompson, S. van der Marck, L. Welser-Sherrill, D. Wiarda, M. White, J.L. Wormald, R.Q. Wright, M. Zerkle, G. Žerovnik, Y. Zhu, *Nucl. Data Sheets* 148 (2018) 1–142, <https://doi.org/10.1016/j.nds.2018.02.001>.
- [6] U. Fasoli, A. Metellini, D. Toniolo, G. Zago, *Nucl. Phys. A* 205 (2) (1973) 305–320, [https://doi.org/10.1016/0375-9474\(73\)90212-1](https://doi.org/10.1016/0375-9474(73)90212-1).
- [7] W. Galati, J.D. Brandenberger, J.L. Weil, *Phys. Rev. C* 5 (1972) 1508–1529, <https://doi.org/10.1103/PhysRevC.5.1508>.
- [8] R.O. Lane, R.D. Koshel, J.E. Monahan, *Phys. Rev.* 188 (1969) 1618–1625, <https://doi.org/10.1103/PhysRev.188.1618>.
- [9] L. Drigo, C. Manduchi, G. Moschini, M.T.R. Manduchi, G. Tornielli, G. Zannoni, *Nucl. Phys. A* 181 (1) (1972) 177–188, [https://doi.org/10.1016/0375-9474\(72\)90910-4](https://doi.org/10.1016/0375-9474(72)90910-4).
- [10] A. Langsdorf, R.O. Lane, J.E. Monahan, *Phys. Rev.* 107 (1957) 1077–1087, <https://doi.org/10.1103/PhysRev.107.1077>.
- [11] A. Elwyn, R. Lane, *Nucl. Phys.* 31 (1962) 78–117, [https://doi.org/10.1016/0029-5582\(62\)90730-7](https://doi.org/10.1016/0029-5582(62)90730-7).
- [12] J.R. Vanhoy, S.F. Hicks, H.E. Baber, B.P. Crider, E.E. Peters, F.M. Prados-Estévez, T.J. Ross, M.T. McEllistrem, S.W. Yates, Basic and applied science using monoenergetic pulsed neutron beams from the University of Kentucky Accelerator Laboratory, in: *Proceedings of the AccApp13 Conference*, Brugge, 5–8 August, 2013.

- [13] J.R. Vanhoy, S.F. Hicks, B.R. Champine, B.P. Crider, E. Garza, S.L. Henderson, S.H. Liu, E.E. Peters, F.M. Prados-Estévez, M.T. McEllistrem, T.J. Ross, L.C. Sidwell, J. Steves, S.W. Yates, Differential Cross Sections Measurements at the University of Kentucky Accelerator: Adventures in Analysis, Tech. Rep. 13, NEMEA-7 / CIELO, NEA/NSC/DOC, 2014.
- [14] J.R. Vanhoy, S.F. Hicks, A. Chakraborty, B.R. Champine, B.M. Combs, B.P. Crider, L.J. Kersting, A. Kumar, C.J. Lueck, S.H. Liu, P.J. McDonough, M.T. McEllistrem, E.E. Peters, F. Prados-Estévez, L.C. Sidwell, A.J. Sigillito, D.W. Watts, S.W. Yates, Nucl. Phys. A 939 (2015) 121, <https://doi.org/10.1016/j.nuclphysa.2015.03.006>.
- [15] P.E. Garrett, N. Warr, S.W. Yates, J. Res. Natl. Inst. Stand. Technol. 105 (2000) 141, <https://doi.org/10.6028/jres.105.019>.
- [16] E. Birgersson, G. Lovestam, NeuSDesc neutron source description software manual, Report No. EUR 23794 EN, Joint Research Centre, Institute for Reference Materials and Measurements, 2009.
- [17] J.F. Ziegler, J.P. Biersack, SRIM-2013, <http://www.srim.org>, 2013.
- [18] M. Drosog, Drosog-2000: Neutron Source Reactions and Codes DROSG-2000 of the IAEA version 2.21, Tech. Rep. IAEA-NDS-87 Rev. 8, IAEA, 2003.
- [19] H. Liskien, A. Paulsen, At. Data Nucl. Data Tables 11 (7) (1973) 569, [https://doi.org/10.1016/S0092-640X\(73\)80081-6](https://doi.org/10.1016/S0092-640X(73)80081-6).
- [20] A.D. Carlson, V.G. Pronyaev, D.L. Smith, N.M. Larson, Zhenpeng Chen, G.M. Hale, F.-J. Hamsch, E.V. Gai, Soo-Youl Oh, S.A. Badikov, T. Kawano, H.M. Hofmann, H. Vonach, S. Tagesen, Nucl. Data Sheets 110 (12) (2009) 3215, <https://doi.org/10.1016/j.nds.2009.11.001>.
- [21] G.M. Hale, ENDF/V-II.1 $^1\text{H}(n,n)$ Reaction Evaluation, Tech. Rep., LANL, Dec. 2006.
- [22] J.R. Lilley, MULCAT-BRC, A Monte Carlo Neutron and Gamma-Ray Multiple Scattering Correction Program, Tech. Rep. P2N/934/80, Internal Service de Physique et Techniques Nucleaire, Centre d'Etudes de Bruyeres-le-Chatel, 1980.
- [23] F.G. Perey, W.E. Kinney, Prog. Rep.: US AEC Nucl. Cross Sections Advisory Comm., Repts. EXFOR entry 10609002, Tech. Rep. 42, ORNL, 1978.
- [24] V.C. Rogers, V.J. Orphan, C.G. Hoot, V.V. Verbinski, Gamma-ray production cross sections for carbon and nitrogen from threshold to 20.7 MeV, Nucl. Sci. Eng. 58 (3) (1975) 298–313, <https://doi.org/10.13182/NSE75-A26779>.